Title

Order-of-magnitude SNR improvement for high-field EPR spectrometers via 3D printed quasi-optical sample holders

Journal

Science Advances, 9(38)

ISSN

2375-2548

Authors

Sojka, Antonín

Price, Brad D

Sherwin, Mark S

Publication Date

2023-09-22

DOI

10.1126/sciadv.adi7412

Peer reviewed

APPLIED PHYSICS

Order-of-magnitude SNR improvement for high-field EPR spectrometers via 3D printed quasi-optical sample holders

Antonín Sojka[1,2]*, Brad D. Price[1,2], Mark S. Sherwin[1,2]*

Here, we present a rapidly prototyped, cost-efficient, and 3D printed quasi-optical sample holder for improving the signal-to-noise ratio (SNR) in modern, resonator-free, and high-field electron paramagnetic resonance (HFEPR) spectrometers. Such spectrometers typically operate in induction mode: The detected EPR ("cross-polar") signal is polarized orthogonal to the incident ("co-polar") radiation. The sample holder makes use of an adjustable sample positioner that allows for optimizing the sample position to maximize the 240-gigahertz magnetic field B_1 and a rooftop mirror that allows for small rotations of the microwave polarization to maximize the cross-polar signal and minimize the co-polar background. When optimally tuned, the sample holder was able to improve co-polar isolation by $\gtrsim$20 decibels, which is proven beneficial for maximizing the SNR in rapid-scan, pulsed, and continuous-wave EPR experiments. In rapid-scan mode, the improved SNR enabled the recording of entire EPR spectra of a narrow-line radical in millisecond time scales, which, in turn, enabled real-time monitoring of a sample's evolving line shape.

INTRODUCTION

Electron paramagnetic resonance (EPR) is a spectroscopic technique based on the Zeeman effect. An unpaired electron spin in the presence of external magnet field has two eigenstates: "spin-up" and "spin-down"; irradiating a spin-up electron with a photon of energy equal to the difference between these two states leads to photon absorption and spin excitation (*1*). EPR spectrometers make use of this effect to probe the local environments of electron spins and can be found in a large fraction of chemistry and materials science laboratories, often to study radical species under a variety of conditions (solution, powder, crystal, in cell, etc.) or to characterize electronic materials (*2*–*12*). Nowadays, EPR is also used in the development of novel materials, such as single-molecule magnets (*13*–*17*), single-ion magnets (*18*–*22*), and quantum bits (*23*), and is thus increasing in popularity.

EPR spectrometers most often operate between 10 and 100 GHz (with magnetic fields between 0.35 and 3.5 T for g-factor $g \asymp 2$), with samples in resonant cavities to enhance signal-to-noise ratio (SNR). High-frequency EPR (frequencies above 100 GHz, fields above 3.5 T, "HFEPR"), however, is advantageous for increased resolution and is especially informative for systems that have gaps in their excitation spectra at zero magnetic field, including molecules with spin > $^1/_2$ and large zero-field splitting (*17*, *24*–*26*), collective spin excitations in antiferromagnets (*27*, *28*), and frustrated spin systems (*29*, *30*). HFEPR spectrometers are also invaluable for measuring the spin dynamics of radicals used as polarizing agents in dynamic nuclear polarization–enhanced nuclear magnetic resonance spectrometers, which operate above 7 T (*31*, *32*).

Motivated by the tremendous scientific opportunities at high field, the development of HFEPR spectrometers is an active field of research (*33*–*38*). The well-known challenges of generating powerful electromagnetic radiation in the 100- to 1000-GHz band have resulted in delayed development of HFEPR when compared to low-field EPR. Furthermore, higher frequencies bring additional challenges: Resonant cavities get smaller (*39*–*41*), and, above 200 GHz, most systems do not use a cavity at all, which forfeits the large signal-to-noise improvement that they often provide (*42*–*44*). To achieve sufficient sensitivity without a cavity, HFEPR spectrometers typically operate in induction mode; this means that a wire grid polarizer above the sample ideally only reflects radiation into the detector that is perpendicular to the input polarization. The perpendicular radiation (called "cross-polar") is made of information about the sample, whereas the incident polarization ("co-polar") is made up of almost entirely background. Therefore, maximizing the cross-polar–to–co-polar contrast also means maximizing the spectrometer's sensitivity. While typically capable of isolating the excitation polarization by about 30 dB (*45*, *46*), induction mode architectures still impart an undesirable background to EPR experiments, as the excitation power is typically much larger than the orthogonal induction-mode signal; as a result, improving induction-mode isolation for high-field and high-frequency experiments presents a potential avenue for improving HFEPR resolution and is a topic of interest for many researchers (*37*, *47*–*52*).

Most EPR systems operate in one (or more) of three modes: continuous-wave (cw), where the field is slowly swept through the resonance, either by frequency or field; pulsed, with a fixed field and frequency that can obtain electron spin-lattice (T_1) or spin-spin (T_2) relaxation times as well as small hyperfine and dipolar couplings; or rapid-scan, where a rapid, continuously averaged sweep of field or frequency through the resonance distorts the spectrum and provides the slow-scan line shape with higher-than-cw SNR (*53*) as well as T_2 relaxation time through postprocessing (see Fig. 1). Rapid-scan EPR can also be used to monitor the kinetics of molecular processes by recording entire spectra as a function of time. Such kinetic studies have been recently implemented at 9.5 GHz to study, for example, intracellular protein–lipid interactions (*54*, *55*) and the

[1]Department of Physics, University of California, Santa Barbara, Santa Barbara, CA, USA. [2]Institute for Terahertz Science and Technology, University of California, Santa Barbara, Santa Barbara, CA 93106, USA.
*Corresponding author. Email: antonin_sojka@ucsb.edu (A.S.); sherwin@ucsb.edu (M.S.S.)

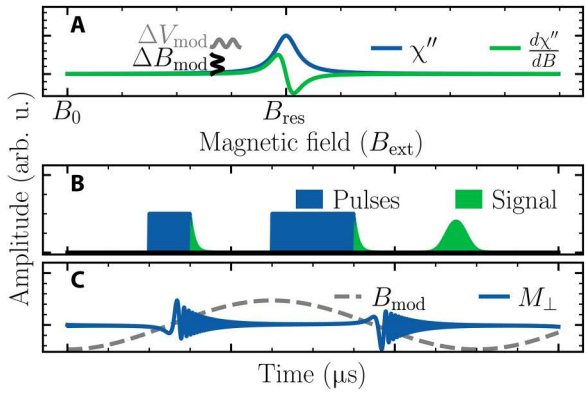

Fig. 1. Simulated signals for cw, pulsed, and rapid-scan EPR. (**A**) In cwEPR, the external magnetic field is modulated (B_{mod}) by a coil, and the EPR signal is detected by a lock-in amplifier (resulting modulated signal is V_{mod}). The resulting EPR signal (green) is the derivative of the imaginary part of the complex magnetic susceptibility (χ'', blue). (**B**) Pulsed EPR uses short driving pulses (blue) to excite spins out of equilibrium and probe their dynamics; in the Hahn echo experiment shown here, the first pulse rotates the net magnetization of the spins, and a second pulse refocuses their precession in the rotating frame, resulting in a spin echo (green). (**C**) Rapid-scan EPR uses fast, large-amplitude modulation (black dashed line) through the resonance and direct-detection of the induction mode signal to record the response of the spins (blue solid line). Fast repetition and continuous signal averaging can allow for better SNR after shorter acquisition time than conventional cwEPR (*52*). arb. u., arbitrary units.

aggregation of intrinsically disordered proteins. To our knowledge, no kinetic studies using rapid-scan EPR have been performed in a very high-field EPR spectrometer (above 100 GHz). However, recent studies using cwEPR at 8.6 T (240 GHz) to detect motion between residues in a photosensitive protein (*52*) motivated the authors of this work to develop high-sensitivity, high-field, and rapid-scan EPR to observe entire dipolar-broadened line shapes during their evolution in time.

Here, we report a frequency-independent high-field sample holder that enables an important improvement in SNR for HFEPR spectrometers that is easy to design, prototype, and implement. The quasi-optical sample holder (QSH) presented here, designed to operate in all three modes (cw, pulsed, and rapid-scan), was fitted to attach to the EPR probe used in EPR spectrometer at the Institute for Terahertz Science and Technology (ITST). Minor adjustments to the 3D printed model (.stp files included in the Supplementary Materials) would allow for simple incorporation into other probe designs. The QSH was entirely 3D printed for rapid prototyping, except for the 12.7 mm diameter parabolic mirror (focal length of 25.4 mm), which was purchased from Thorlabs Inc., and the rooftop mirror, which was end-milled from a 7-mm-diameter aluminum rod (see fig. S1). Using the QSH, we demonstrate an enhanced SNR in three EPR modes. For cwEPR, the enhanced SNR provides equal sensitivity with fewer spins. For pulsed EPR, it reduces undesirable co-polar power enough that direct measurements of cross-polar power can immediately return a field-swept EPR spectrum without requiring an engineered pulse sequence. For rapid-scan EPR, the SNR enhancement enables time-resolved kinetic studies with tunable time resolution (currently down to 15 ms).

RESULTS

Design of sample holder

We discuss two types of sample holders throughout this manuscript: the "simple" sample holder (SSH) and our QSH. A body similar to the SSH can be found in almost any HFEPR lab and is, therefore, a useful comparison to the QSH. The SSH typically consists of two parts that are machined from plastic: One is permanently attached to the corugated waveguide and supports the modulation coil, and the other is a detachable insert on which the sample sits. By varying the insert's length, the sample can be placed close to the corrugated waveguide output at the top of the modulation coil (Fig. 2, "SSH-T") or in the center of the modulation coil (Fig. 2, "SSH-M"). In both SSH configurations, the sample sits directly on a planar mirror that reflects incident radiation back into a corrugated waveguide. For pulsed EPR, the SSH-T position is used to minimize microwave loss due to divergence of the propagating Gaussian beam. For rapid-scan EPR and cwEPR, the SSH-M position is used to obtain the largest and maximally homogeneous modulation field at the sample space.

The QSH was designed with a broad range of applications and user-friendliness in mind. Our frequency-independent design for the QSH uses focusing quasi-optics to ensure that the beam waist is kept within the sample holder's specified optical path, reducing microwave beam clipping due to the waveguide aperture. The quasi-optical design does not require a waveguide or end mirror within its modulation coil, which eliminates eddy currents inside the coil, and results in an improvement of field modulation amplitude and homogeneity. The quasi-optics consist of a 25.4 mm focusing parabolic mirror (MPD019-M03, Thorlabs Inc., USA) mounted along the axis of the corrugated waveguide and a rooftop mirror machined using an end mill. A simulation of quasi-optical fundamental mode Gaussian beam propagation is shown in Fig. 3 (*56*). These simulations show the beam waist compared to the quasi-optical elements and highlight that clipping loss is reduced due to the focusing quasi-optics.

The QSH was designed for 3D printing (printer details in Materials and Methods) and room temperature operation and works well in these conditions. With a different printing substrate (e.g., nylon-based filament), liquid nitrogen temperatures should be easily achievable (*57*). If higher precision or durability is required, then a QSH could be made using subtractive machining after a design has been prototyped and finalized via 3D printing.

Mechanical transmission systems to increase cross-polar isolation and maximize desired EPR signal

To motivate the design of the QSH, it is instructive to first review the design of the ITST 240-GHz EPR spectrometer, which is typical of quasi-optical HFEPR spectrometers. A wire grid polarizer at the end of the quasi-optical bridge reflects the polarized 240-GHz radiation into a 1.2-m gold-plated corrugated waveguide that is coupled to the sample space. On resonance, the radiation that is reflected by the sample acquires a small, orthogonally polarized component (cross-polar) that is the EPR signal of interest. This signal is reflected by a wire grid at the end of the bridge, received by a WR3.4 Schottky diode–based subharmonic mixer (Virginia Diodes Inc.), and subsequently mixed down to 10 GHz (see Fig. 4). The 10-GHz signal must be limited to no more than −35 dBm to avoid saturating intermediate frequency (IF) stage mixers and distorting the resulting EPR signal. Ideally, all the co-polar radiation is directed

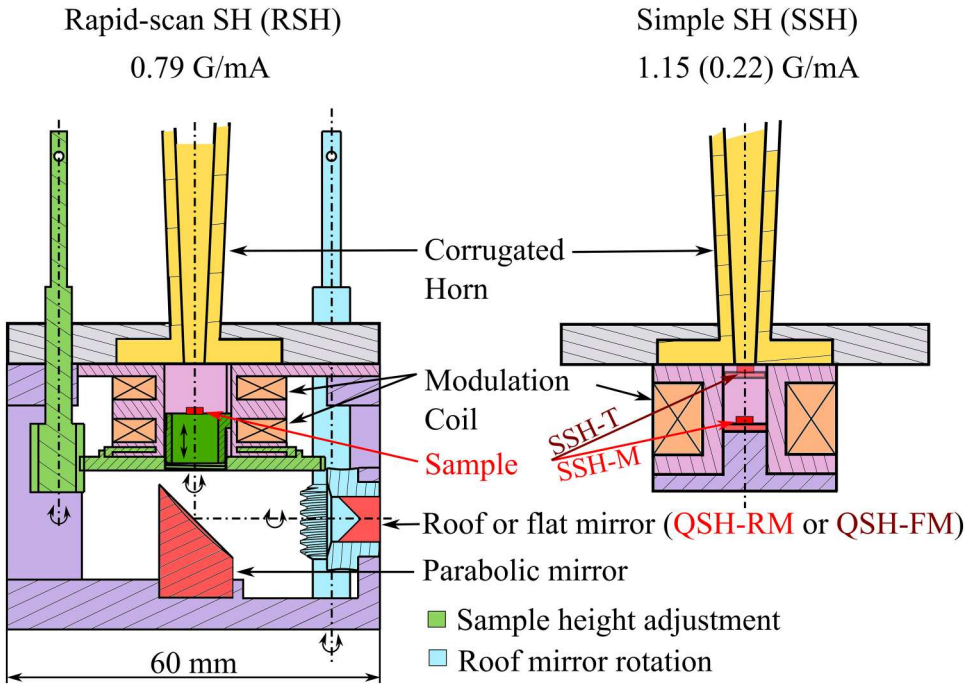

Fig. 2. Schematic drawing of QSH and SSH. The SSH has been used at ITST previously with two sample positions: the middle of the coil to maximize modulation amplitude (SSH-M) and the top of the coil to minimize losses due to divergence of the 240-GHz Gaussian beam (SSH-T). The QSH uses one of two end mirrors: a rooftop mirror (RM) or a flat mirror (FM) and uses two mechanical adjustment knobs: one to optimize sample position along the optical axis (green) and one to rotate the rooftop mirror to optimize cross-polar isolation (blue). The sample is positioned using a spur gear assembly with a 5:1 gear ration. The rooftop mirror is rotated by a worm gear assembly with a 30:1 gear ratio.

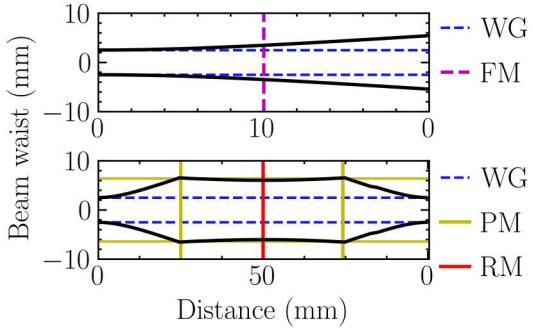

Fig. 3. Simulation of Gaussian beam propagation through both sample holders. The black lines denote a circle that encloses 99% of the energy in the beam (*56*). The thin dotted blue lines represent the diameter of the input waveguide. The beams are reflected by a mirror at the middle of each propagation path. (**Top**) In the SSH-M, after reflection from a flat mirror at x = 10 mm (FM; dashed purple line), the beam expands to a size larger than waveguide (WG; dashed blue line) that results in microwave losses. (**Bottom**) In the QSH, the beam expands after leaving the end of the waveguide (dashed blue lines) at millimeters and is focused by parabolic mirror of 12.7-mm diameter (PM; solid yellow lines) onto the roof mirror at x = 51.8 mm (RM; solid red line) and then back the waveguide along the same path. Because the sample dimensions are small compared to the beam, we neglect a small shift of beam waist position at the output of the corrugated taper as well as any higher order Gaussian beam modes that are produced as a result of parabolic mirror aberrations (*56*).

back toward the source and does not reach the receiver. However, without the rooftop mirror, enough co-polar radiation reaches the receiver that both the signal and co-polar leakage must be attenuated by a variable attenuator (the details about the roof mirror physics are in section S1). This attenuation degrades the SNR, especially if the noise from subsequent IF amplifiers is greater than the noise of the attenuated IF signal (further discussion in section S2). Although it depends largely on the absorptive properties, size, and thickness of a given sample, most SSH experiments require the attenuator to be set between 15 and 25 dB.

If a sample is thin compared to the wavelength, then the EPR signal is maximized by placing it at an antinode of the microwave's magnetic field (B_1). Thus, two independent adjustments are necessary: one to rotate the roof mirror to minimize co-polar leakage and one to translate the sample to a maximum of B_1.

Roof mirror rotation and sample translation are implemented with two mechanical transmission systems (see fig. S2). The first system rotates the rooftop mirror about an axis perpendicular to the magnetic field; as reported by previous work, subdegree rotation of a rooftop end mirror can result in approximately 30 dB of additional cross-polar isolation (*46*, *47*). To achieve subdegree precision, a 30:1 worm gear assembly was used. The worm gear pinion is connected to a lead that ends outside of the magnet and can be rotated by hand or a connected stepper driver. The co-polar and cross-polar signal amplitudes as a function of roof-mirror angle are shown in fig. S4. When using the rooftop end mirror (*47*), the cross-polar isolation is greatly improved, and the variable attenuator can be adjusted to attenuate much less IF power down to 0 dB while still limiting power to the IF stage to −35 dBm.

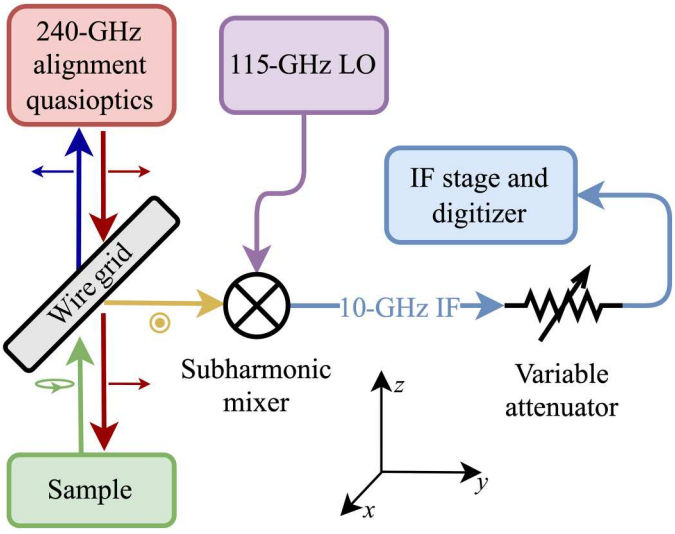

Fig. 4. Schematic drawing demonstrating ITST's heterodyne detection scheme for induction mode EPR. Co-polar, *y*-polarized 240-GHz microwaves (red line) enter the waveguide through a wire grid polarizer with wires oriented along the *x* axis and propagate along the waveguide polarized in the *y* direction (red line). Reflected microwaves are slightly elliptically polarized in the *xy* plane (green line). The cross-polar, *x*-polarized microwaves (yellow line) are reflected by the wire grid polarizer and received by the WR3.4 Schottky diode–based subharmonic mixer (Virginia Diodes Inc.), while the co-polar microwaves (blue line) are transmitted back through the wire grid into an absorber. Cross-polar microwaves are mixed down to 10 GHz (blue line) by a 115-GHz local oscillator (purple rectangle and line). A variable attenuator limits the intermediate frequency (IF) power so that approximately −35 dBm of 10 GHz signal is transferred to the IF stage for filtering, amplification, additional mixing, and digitization. The polarization state of the beam in each path is depicted by small arrows.

The second transmission system positions the sample at a maximum of B_1 using a 5:1 spur gear assembly rotating about an axis parallel to the magnetic field. The sample rests on 12.7-μm-thick Mylar film that is glued to a slot-guided, threaded shaft. Rotation of the spur gear is translated into linear motion of the M10x0.5 threaded shaft along the applied microwave axis (see fig. S3). Translation along the microwave axis is not necessary in the case of the SSH, as the standing-wave condition ensures that an electric field node (and, hence, a magnetic field antinode) appears on the surface of the mirror.

Experimental results

The QSH was tested with three different samples and EPR modes (see Table 1): a solution of 100 μM gadolinium chloride in D_2O by cwEPR as a proxy for Gd spin labels used for distance measurements in spin-labeled proteins (*58*), a diamond crystal with nitrogen substitutional defects (P1 centers) by pulsed EPR as a proxy for solid-state spin qubit candidates, and a single crystal of lithium phthalocyanine (LiPc) by rapid-scan EPR as a narrow-line radical that is sensitive the local oxygen concentration (*59*). The measurements were compared with those done with the SSH, in both the SSH-M and SSH-T positions. The QSH experiments were done with a flat (QSH-FM) and rooftop end mirror (QSH-RM) for comparison. Optimization procedure for each experiment using the QSH-RM is described in detail in section S3.

cwEPR

cwEPR was performed on 100 μM $GdCl_3$ dissolved in D_2O. The $GdCl_3$ solution was inserted into a 100-μm-thick, 2 mm–by–5 mm borosilicate glass capillary (VitroCom, Mountain Lakes, NJ, USA) to maximize the ratio of surface area to thickness and sealed with wax (*60*). The modulated signal was amplified using a lock-in detector (SR830, Stanford Research Systems) and is shown in Fig. 5. The SNR was best in the case of QSH-RM (SNR = 292) because of our ability to minimize the co-polar baseline while also maximizing the spin response by optimizing the sample position. Next best was SSH-T (SNR = 53), due to the near-zero microwave losses as a result of the mirror being placed directly at the end of the waveguide. SSH-M had the lowest SNR (SNR = 14): This is due to microwave losses as a result of divergence of the Gaussian beam. QSH-FM (SNR = 37) had an SNR greater than that of SSH-M because it was able to reduce divergence loss with focusing quasi-optics but, as expected, still had more divergence loss than SSH-T, which had no free-space propagation.

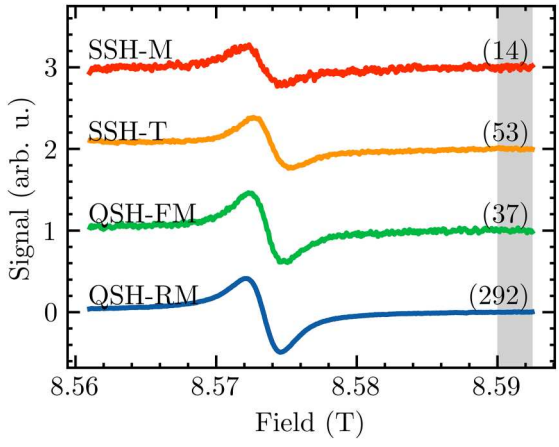

Fig. 5. cwEPR of 100 μM GdCl3. EPR signal as a function of field, as detected by a lock-in amplifier (100-ms lock-in time constant). The applied magnetic field was modulated at the resonant frequency of the modulation coil and an accompanying 10-nF capacitor (B_{mod} = 14.8 G at 33 kHz in the case of the SSH and B_{mod} = 7.9 G at 23 kHz in the case of the QSH). The SNR was best in the case of the QSH-RM (blue) because of the ability to reduce co-polar noise, as well as to position the thin $GdCl_3$-filled capillary at a maximum of the irradiated B_1 field. The baseline was removed by subtracting the mean of points within the vertical gray column. SNR (in parentheses) was calculated by dividing peak baseline-corrected signal by the SD of baseline-corrected points within the vertical gray column.

Table 1. SNR and insertion loss for each sample holder configuration. SH config., sample holder configuration; CW, continuous wave; RS, rapid scan; Ins. loss, insertion loss; P1 dia., P1 diamond.

SH config.	CW	Pulsed	RS	Ins. loss (dB)
Sample	Gd(III)	P1 dia.	LiPc	–
SSH-M	14	178	278	4.18 ± 0.2
SSH-T	53	472	–	2.67 ± 0.4
QSH-FM	37	219	788	1.84 ± 0.6
QSH-RM	292	524	1620	1.53 ± 0.4

Pulsed EPR

Pulsed EPR was performed at 240 GHz on P1 nitrogen vacancy centers in a diamond crystal using a cw 60-mW source Virginia Diodes, Inc. that was pulsed using a fast PIN (p-type, intrinsic, n-type) diode switch (SWM-0JV-1DT-2ATT, American Microwave Corporation, USA). A Hahn echo pulse sequence, consisting of a 600-ns excitation pulse, 1.2-μs delay time, and 800-ns refocusing pulse, was used to create a spin echo. The pulse sequence was repeated at 1 kHz and averaged over 512 repetitions per field position. Integrated echo intensity was recorded as a function of field and plotted in Fig. 6. The results from each sample holder were quite similar. The SSH-M performed the worst (SNR = 178) because its long optical path length and beam divergence cause clipping at the waveguide aperture (see Fig. 3). The SSH-T did not suffer from this clipping and, therefore, performed second best (SNR = 472). The QSH-FM (SNR = 219) and the QSH-RM (SNR = 524) should have performed similarly, as the co-polar background cannot obscure the cross-polar signal after the pulse sequence has occurred. However, optimizing the roof mirror angle for the maximum Hahn echo did improve SNR and allowed the QSH-RM to perform the best overall.

Rapid-scan EPR

Rapid-scan EPR was performed on a needle of LiPc at 240 GHz in three sample holders (SSH-M, QSH-FM, and QSH-RM). Rapid-scan SSH-T experiments were not performed because the modulation field strength (approximately 16-gauge tip to trough; see section S4) was insufficient to entirely sweep the LiPc resonance. The rooftop mirror increased the cross-polar isolation by ~20 dB. As shown in Table 1 and Fig. 7, the SNR of the QSH represented an improvement over the SSH. In the QSH-FM, the SNR improved by approximately 3× over the SSH-M (278 → 788). After replacing the end mirror with a rooftop mirror (QSH-RM), the SNR was improved by an additional 2× (788 → 1620), for a total improvement of 6× (278 → 1620).

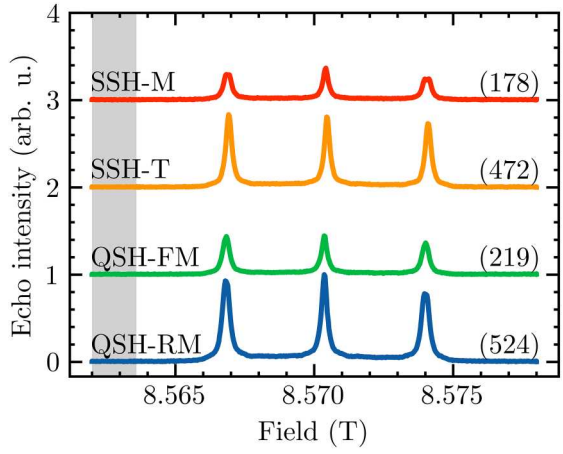

Fig. 6. Field-swept echo of P1 centers in diamond. Integrated echo magnitudes plotted as a function of field for each sample holder configuration (1 kHz repetition rate with 512 averages at each field position). SSH-M (red) performed the worst (SNR = 178). SSH-T (orange) performed as the second best; the optical path length was minimal and, therefore, so were losses due to propagation (SNR = 472). QSH-FM (green) performed second worst (SNR = 219). QSH-RM (blue) performed the best as a result of focusing optics and the ability to maximize desirable cross-polar signal (SNR = 524). SNR (in parentheses) was calculated by dividing peak signal by the SD of points within the vertical gray column.

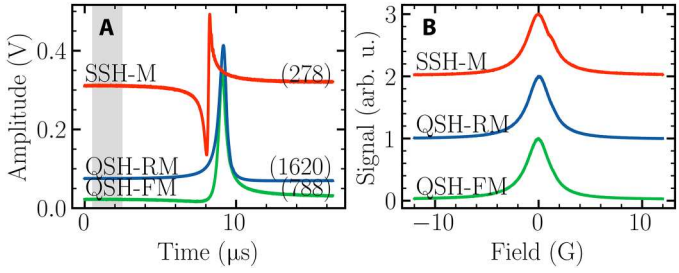

Fig. 7. Rapid-scan EPR of LiPc needle, directly detected and averaged. (**A**) Time-resolved rapid-scan EPR spectra of LiPc with 10,000 averages. SSH-M is shown in red (B_{mod} = 144 G at 33 kHz, variable IF attenuator setting A_{var} = 25.5 dB, SNR = 278); QSH-FM is shown in green, and sample position was adjusted using the optical axis positioning thread to maximize signal amplitude (B_{mod} = 75 G at 23 kHz, A_{var} = 20.5 dB, SNR = 788); QSH-RM is shown in blue, sample position was adjusted using the optical axis positioning thread to maximize signal amplitude, and the rooftop mirror was adjusted to minimize co-polar baseline (B_{mod} = 75 G at 23 kHz, A_{var} = 5.75 dB, SNR = 1620). SNR (in parentheses) was calculated by dividing peak amplitude by the root mean square deviation of points within the vertical gray bar. (**B**) Deconvolved LiPc spectra after application of the driving-function Fourier deconvolution algorithm found in (*64*).

DISCUSSION

Here, we demonstrated a rapidly prototyped, cost-efficient 3D printed sample holder that is capable of greatly improving the SNR of cwEPR and rapid-scan EPR by reducing co-polar leakage and optimizing B_1 field strength at the sample position. The sample holder presented here represents an easy-to-implement solution for improving the SNR of a variety of homebuilt EPR spectrometer designs through custom-fit modifications of the .stp files included in the Supplementary Materials. 3D printed components enable simple incorporation into a variety of induction mode HFEPR spectrometers and provide a method to improve SNR while still allowing further customization for possible additional functionality. The three main benefits of our design can be summarized as follows.

1) Better SNR and sensitivity improvement: The QSH showed SNR improvements for all three EPR experimental techniques: cw, rapid-scan, and pulsed (see Table 1). In the case of cwEPR and rapid-scan EPR, reducing the baseline is critical for improving the SNR. In this case, the rooftop mirror provides a substantial benefit. It can improve co-polar isolation by ≳20 dB and SNR by around 6, when compared to the best possible configuration using the SSH. In addition, the QSH benefited from cwEPR and rapid-scan EPR by allowing the sample to be placed in the middle of the modulation coil where the best possible performance could be achieved. Note that the results presented here were established using an imperfect rooftop mirror end-milled from an aluminum rod.

2) Reduction of co-polar intensity during pulsed EPR measurements: In pulsed EPR, the signal is usually detected after the excitation is turned off, which makes co-polar leakage a smaller concern than in the other two modes. Therefore, in this mode, the sample is typically placed as close as possible to the waveguide to limit losses due to Gaussian beam propagation. Such losses cannot be avoided in the QSH-FM/RM, but they can be partially mitigated by the parabolic focusing mirrors. Nevertheless, even for the Hahn echo

experiment presented here, the QSH-RM was able to improve SNR by ~11%. To achieve this improvement, the polarization of the echo was slightly rotated to better couple with the induction mode quasi-optics, and the sample was positioned at a magnetic field antinode.

For high-power pulsed HFEPR measurements, in which the microwave pulse is generated by a gyrotron or free-electron laser, improved cross-polar isolation should greatly reduce the time between the end of the pulse sequence and the time at which detection of an echo or free-induction decay begins (often called the "dead time"). As an illustration, Fig. 8 shows experiments in which a pulsed EPR signal from P1 centers in diamond is recorded during a 240-GHz microwave pulse from our amplifier-multiplier chain—a so-called "zero–dead time" experiment (*47*). With the SSH, which has no roof mirror, the co-polar signal dominates, resulting in a large baseline, and the features associated with P1 centers show up as a decrease in the signal. When using the QSH with the roof mirror properly adjusted, the baseline associated with co-polar leakage is reduced enough that the cross-polar EPR signal dominates and sample absorption is directly observed as an enhancement of detected pulse power, returning the expected EPR spectrum.

3) Enables real-time rapid-scan EPR of transient phenomena: The QSH improved co-polar isolation by a factor of ≳20 dB and SNR by approximately 6, corresponding to a 36× reduction in signal acquisition time for comparable SNR. For rapid-scan experiments, a reduction in requisite acquisition time increases the time resolution, enabling capture of more rapid transient phenomena. As a proof of concept, we "filmed" the well-known line broadening of the EPR spectrum of a LiPc needle under oxygenic conditions (*59*, *61*). The sample space was pressurized (<4 psi) by a continuous flow of nitrogen gas for 5 min and then quickly switched to a continuous flow of air (<4 psi). A set of spectra recorded at different times, in the left panel of Fig. 9, shows the expected broadening. The right panel shows the linewidth as a function of time, extracted from Lorentzian fits to a set of ~400 sequentially acquired spectra, showing the onset of broadening when oxygen reaches the crystal. In this case, we achieved the sensitivity required to observe the broadening due to oxygenation with time steps as low as 15 ms, although each point plotted here was averaged over 300 ms.

Future work for the QSH-RM includes incorporating a fast-loading sample design and identifying and optimizing a 3D printing substrate that is capable of handling liquid nitrogen temperatures for cryogenic experiments (*57*, *62*). It may also be beneficial to implement a piezo-electric rotator in place of the manual rotation knob to optimize sample position and rooftop mirror angle automatically and repeatably. Furthermore, the QSH may provide an avenue to greatly reduce dead time of pulsed EPR using high-power microwave sources such as ITST's free electron laser (*35*). Last, rapid-scan EPR of proteins doubly labeled with Gd spin tags offers the possibility of "filming" proteins in action by measuring dipolar-broadened EPR spectra as a function of time (*58*). Although experiments performed here were done without a cavity, the QSH-RM sample holder should be compatible with a Fabry-Pérot type cavity, which would further enhance SNR and time resolution.

MATERIALS AND METHODS

Fabrication of QSH

The prototype and gears were 3D printed from polylactic acid by an Original Prusa i3 MK3S+ (Prusa Research s.r.o., Czech Republic).

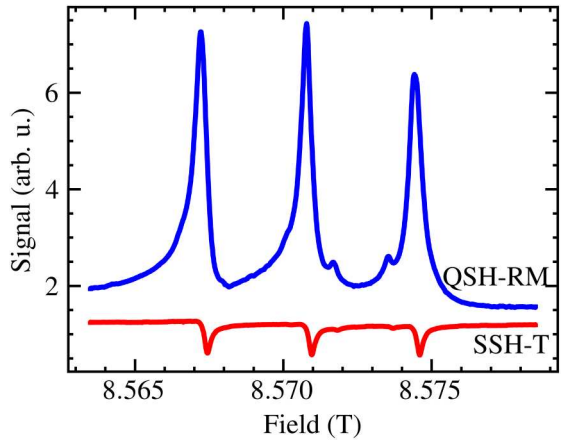

Fig. 8. Integrated intensity of a long (~1 μs) microwave pulse during a resonant field sweep. In the case of the SSH-T, the resonant signal is a result of a decrease of the detected co-polar power due to substantial leakage. After optimization, the QSH-RM signal is primarily cross-polar and thus results in a signal increase while on resonance.

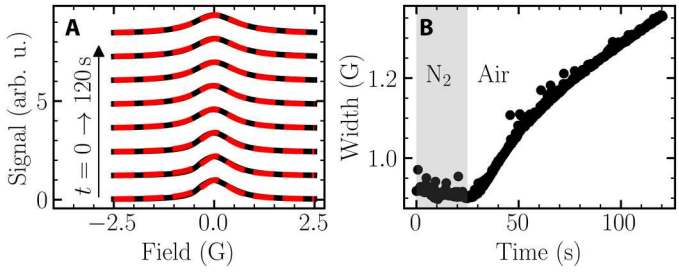

Fig. 9. Line shape broadening of a LiPc needle due to oxygenation. (**A**) Individual "frames" of the time-resolved rapid-scan line shape. The time elapsed between each frame shown was ~15 s, although a similar frame was recorded every ~300 ms. Frames of ~15 ms (250 scans) provided sufficient SNR for filming, but frames of ~300 ms (5000 scans) were more than fast enough to resolve this minute-long process. Raw data are shown in black, and a Lorentzian best fit is show in dashed red. (**B**) Lorentzian linewidth as a function of time as returned by least-squares best fit [fit shown in red in (A)]. Nitrogen atmosphere is represented by the gray background; air atmosphere is represented by the white background. Infrequent outlier points may be due to turbulent air within the sample space or imperfect programmatic signal phasing in postprocessing.

We used a Helmholtz modulation coil wound from Cu 32 American Wire Gauge wire to get direct access to the sample space. Sample space access is necessary for fiber optical excitation in experiments similar to those presented in (*58*) and may also allow for fast sample loading in future designs. The coil was calibrated using a reference sample of LiPc (see fig. S6).

Measurement of insertion losses

The insertion losses mentioned in Table 1 were measured with a quasi-optical THz detector (3DL 12C LS2500 A2, ACST GmbH, Germany). The detector was set up to measure the returned co-polar intensity (*y* axis polarized blue signal in Fig. 7) that should represent the entirety of the source power (except insertion loss) after reflection from an empty sample holder. The QSH was tuned to maximize the amount of co-polar power detected in this

configuration. The control experiment for normalization was done with a planar mirror placed directly before the EPR probe input.

Samples

P1 diamond

The diamond sample was a 5 mm–by–5 mm–by–1 mm type 1b diamond crystal with substitutional nitrogen ("P1") defects. Estimated P1 concentration is approximately 62 ± 5 parts per million (*58*). The crystal was adhered to its mount using Apiezon vacuum grease.

Gadolinium(III) chloride

Gadolinium chloride was bought from Sigma-Aldrich and dissolved in D_2O with a concentration of 1 mM and then diluted to 100 μM. The spectra shown in Fig. 4 were recorded without sample degassing. The capillary rested on its mount and stayed in position due to gravity.

Lithium phthalocyanine

LiPc in microcrystalline form was prepared electrochemically following a procedure described in the literature (*59*, *63*). A crystal sample was obtained from Mark Tseytlin (West Virginia University). A sharp single needle was adhered to its mount using Apiezon vacuum grease.

Statistical analysis

SNR was calculated for all spectra by dividing the peak amplitude of each signal by the SD of points within the gray vertical bars.

Supplementary Materials

This PDF file includes:
Sections S1 to S5
Figs. S1 to S6
Table S1
Legend for data S1
References

Other Supplementary Material for this manuscript includes the following:
Data S1

REFERENCES AND NOTES

1. J. A. Weil, J. R. Bolton, *Electron Paramagnetic Resonance: Elementary Theory and Practical Applications* (John Wiley & Sons, 2007).
2. J. H. Freed, Electron spin resonance. *Annu. Rev. Phys. Chem.* **23**, 265–310 (1972).
3. F. J. Owens, Paramagnetic resonance studies of phase transitions in condensed materials. *Phase Transit.* **5**, 81–137 (1985).
4. M. Farle, K. Baberschke, Ferromagnetic order and the critical exponent gamma for a Gd monolayer: An electron-spin-resonance study. *Phys. Rev. Lett.* **58**, 511–514 (1987).
5. M. Che, E. Giamello, "Electron paramagnetic resonance," in *Studies in Surface Science and Catalysis* (Elsevier, 1990), chap. 5.
6. J. H. Freed, New technologies in electron spin resonance. *Annu. Rev. Phys. Chem.* **51**, 655–689 (2000).
7. B. Gallez, C. Baudelet, B. F. Jordan, Assessment of tumor oxygenation by electron paramagnetic resonance: Principles and applications. *NMR Biomed.* **17**, 240–262 (2004).
8. L. M. B. Napolitano, O. R. Nascimento, S. Cabaleiro, J. Castro, R. Calvo, Isotropic and anisotropic spin-spin interactions and a quantum phase transition in a dinuclear Cu(II) compound. *Phys. Rev. B.* **77**, 214423 (2008).
9. M. J. Davies, Detection and characterisation of radicals using electron paramagnetic resonance (EPR) spin trapping and related methods. *Methods* **109**, 21–30 (2016).
10. K.-R. Naveed, L. Wang, H. Yu, R. Summe Ullah, M. Haroon, S. Fahad, J. Li, T. Elshaarani, R. Ullah Khan, A. Nazir, Recent progress in the electron paramagnetic resonance study of polymers. *Polym. Chem.* **9**, 3306–3335 (2018).
11. S. A. Bonke, T. Risse, A. Schnegg, A. Brückner, In situ electron paramagnetic resonance spectroscopy for catalysis. *Nat. Rev. Methods Primer.* **1**, 33 (2021).
12. A. Bonucci, O. Ouari, B. Guigliarelli, V. Belle, E. Mileo, In-Cell EPR: Progress towards Structural Studies Inside Cells. *Chembiochem* **21**, 451–460 (2020).
13. S. Hill, S. Maccagnano, K. Park, R. M. Achey, J. M. North, N. S. Dalal, Detailed single-crystal EPR line shape measurements for the single-molecule magnetsFe8BrandMn12−acetate. *Phys. Rev. B.* **65**, 224410 (2002).
14. A. Schnegg, J. Behrends, K. Lips, R. Bittl, K. Holldack, Frequency domain Fourier transform THz-EPR on single molecule magnets using coherent synchrotron radiation. *Phys. Chem. Chem. Phys.* **11**, 6820–6825 (2009).
15. S. Datta, E. Bolin, R. Inglis, C. J. Milios, E. K. Brechin, S. Hill, A comparative EPR study of high- and low-spin Mn6 single-molecule magnets. *Polyhedron.* **28**, 1788–1791 (2009).
16. S. Ghosh, S. Datta, L. Friend, S. Cardona-Serra, A. Gaita-Ariño, E. Coronado, S. Hill, Multi-frequency EPR studies of a mononuclear holmium single-molecule magnet based on the polyoxometalate $[Ho^{III}(W_5O_{18})_2]^{9-}$. *Dalton Trans.* **41**, 13697–13704 (2012).
17. M. S. Fataftah, S. L. Bayliss, D. W. Laorenza, X. Wang, B. T. Phelan, C. B. Wilson, P. J. Mintun, B. D. Kovos, M. R. Wasielewski, S. Han, M. S. Sherwin, D. D. Awschalom, D. E. Freedman, Trigonal bipyramidal V3+ complex as an optically addressable molecular qubit candidate. *J. Am. Chem. Soc.* **142**, 20400–20408 (2020).
18. L. Sun, S. Zhang, S. Chen, B. Yin, Y. Sun, Z. Wang, Z. Ouyang, J. Ren, W. Wang, Q. Wei, G. Xie, S. Gao, A two-dimensional cobalt(II) network with a remarkable positive axial anisotropy parameter exhibiting field-induced single-ion magnet behavior. *J. Mater. Chem. C.* **4**, 7798–7808 (2016).
19. S. Realista, A. J. Fitzpatrick, G. Santos, L. P. Ferreira, S. Barroso, L. C. J. Pereira, N. A. G. Bandeira, P. Neugebauer, J. Hrubý, G. G. Morgan, J. van Slageren, M. J. Calhorda, P. N. Martinho, A Mn(iii) single ion magnet with tridentate Schiff-base ligands. *Dalton Trans.* **45**, 12301–12307 (2016).
20. K. S. Pedersen, A.-M. Ariciu, S. McAdams, H. Weihe, J. Bendix, F. Tuna, S. Piligkos, Toward molecular 4f single-ion magnet qubits. *J. Am. Chem. Soc.* **138**, 5801–5804 (2016).
21. M. D. Jenkins, Y. Duan, B. Diosdado, J. J. García-Ripoll, A. Gaita-Ariño, C. Giménez-Saiz, P. J. Alonso, E. Coronado, F. Luis, Coherent manipulation of three-qubit states in a molecular single-ion magnet. *Phys. Rev. B.* **95**, 064423 (2017).
22. G. Handzlik, M. Magott, M. Arczyński, A. M. Sheveleva, F. Tuna, S. Baran, D. Pinkowicz, Identical anomalous Raman relaxation exponent in a family of single ion magnets: Towards reliable Raman relaxation determination? *Dalton Trans.* **49**, 11942–11949 (2020).
23. E. Coronado, Molecular magnetism: From chemical design to spin control in molecules, materials and devices. *Nat. Rev. Mater.* **5**, 87–104 (2020).
24. K. A. Earle, D. E. Budil, J. H. Freed, 250-GHz EPR of nitroxides in the slow-motional regime: Models of rotational diffusion. *J. Phys. Chem.* **97**, 13289–13297 (1993).
25. Y. S. Lebedev, Very-high-field EPR and its applications. *Appl. Magn. Reson.* **7**, 339–362 (1994).
26. K. K. Andersson, P. P. Schmidt, B. Katterle, K. R. Strand, A. E. Palmer, S.-K. Lee, E. I. Solomon, A. Gräslund, A.-L. Barra, Examples of high-frequency EPR studies in bioinorganic chemistry. *JBIC J. Biol. Inorg. Chem.* **8**, 235–247 (2003).
27. S. Foner, High-field antiferromagnetic resonance in Cr_2O_3. *Phys. Rev.* **130**, 183–197 (1963).
28. J. Li, C. B. Wilson, R. Cheng, M. Lohmann, M. Kavand, W. Yuan, M. Aldosary, N. Agladze, P. Wei, M. S. Sherwin, J. Shi, Spin current from sub-terahertz-generated antiferromagnetic magnons. *Nature* **578**, 70–74 (2020).
29. S. B. Oseroff, Magnetic susceptibility and EPR measurements in concentrated spin-glasses: $Cd_{1-x}Mn_xTe$ and $Cd_{1-x}Mn_xSe$. *Phys. Rev. B.* **25**, 6584–6594 (1982).
30. H. Martinho, N. O. Moreno, J. A. Sanjurjo, C. Rettori, A. J. García-Adeva, D. L. Huber, S. B. Oseroff, W. Ratcliff, S.-W. Cheong, P. G. Pagliuso, J. L. Sarrao, G. B. Martins, Magnetic properties of the frustrated antiferromagnetic spinel $ZnCr_2O_4$ and the spin-glass $Zn_{1-x}Cd_xCr_2O_4$ (x = 0.05, 0.10). *Phys. Rev. B.* **64**, 024408 (2001).
31. B. D. Armstrong, D. T. Edwards, R. J. Wylde, S. A. Walker, S. Han, A 200 GHz dynamic nuclear polarization spectrometer. *Phys. Chem. Chem. Phys.* **12**, 5920–5926 (2010).
32. S. A. Walker, D. T. Edwards, T. A. Siaw, B. D. Armstrong, S. Han, Temperature dependence of high field 13C dynamic nuclear polarization processes with trityl radicals below 35 Kelvin. *Phys. Chem. Chem. Phys.* **15**, 15106–15120 (2013).
33. G. R. Eaton, S. S. Eaton, High-field and high-frequency EPR. *Appl. Magn. Reson.* **16**, 161–166 (1999).
34. J. van Tol, L.-C. Brunel, R. J. Wylde, A quasioptical transient electron spin resonance spectrometer operating at 120 and 240 GHz. *Rev. Sci. Instrum.* **76**, 074101 (2005).
35. S. Takahashi, L.-C. Brunel, D. T. Edwards, J. van Tol, G. Ramian, S. Han, M. S. Sherwin, Pulsed electron paramagnetic resonance spectroscopy powered by a free-electron laser. *Nature* **489**, 409–413 (2012).
36. P. Neugebauer, D. Bloos, R. Marx, P. Lutz, M. Kern, D. Aguilà, J. Vaverka, O. Laguta, C. Dietrich, R. Clérac, J. van Slageren, Ultra-broadband EPR spectroscopy in field and frequency domains. *Phys. Chem. Chem. Phys.* **20**, 15528–15534 (2018).

37. A. Sojka, M. Šedivý, O. Laguta, A. Marko, V. T. Santana, P. Neugebauer, High-frequency EPR: Current state and perspectives. *Electron Paramagn. Reson.* **27**, 214–252 (2021).
38. A. Schnegg, "Very-high-frequency EPR," in *eMagRes* (John Wiley & Sons Ltd., 2017), pp. 115–132.
39. M. Rohrer, O. Brügmann, B. Kinzer, T. F. Prisner, High-field/high-frequency EPR spectrometer operating in pulsed and continuous-wave mode at 180 GHz. *Appl. Magn. Reson.* **21**, 257–274 (2001).
40. H. Blok, J. A. J. M. Disselhorst, S. B. Orlinskii, J. Schmidt, A continuous-wave and pulsed electron spin resonance spectrometer operating at 275 GHz. *J. Magn. Reson.* **166**, 92–99 (2004).
41. J. H. Enemark, A. M. Raitsimring, High-field EPR spectroscopy on proteins and their model systems: Characterization of transient paramagnetic states. *J. Am. Chem. Soc.* **131**, 10792–10793 (2009).
42. W. Froncisz, J. S. Hyde, The loop-gap resonator: A new microwave lumped circuit ESR sample structure. *J. Magn. Reson.* **47**, 515–521 (1982).
43. W. M. Walsh Jr., L. W. Rupp Jr., Enhanced ESR sensitivity using a dielectric resonator. *Rev. Sci. Instrum.* **57**, 2278–2279 (1986).
44. R. Tschaggelar, F. D. Breitgoff, O. Oberhänsli, M. Qi, A. Godt, G. Jeschke, High-bandwidth Q-Band EPR resonators. *Appl. Magn. Reson.* **48**, 1273–1300 (2017).
45. J. Chen, T. Maly, Compact, tunable polarization transforming reflector for quasi-optical devices used in terahertz science. *Rev. Sci. Instrum.* **93**, 013102 (2022).
46. A. Sojka, thesis, Brno University of Technology (2022).
47. P. A. S. Cruickshank, D. R. Bolton, D. A. Robertson, R. I. Hunter, R. J. Wylde, G. M. Smith, A kilowatt pulsed 94 GHz electron paramagnetic resonance spectrometer with high concentration sensitivity, high instantaneous bandwidth, and low dead time. *Rev. Sci. Instrum.* **80**, 103102 (2009).
48. E. J. Reijerse, High-frequency EPR instrumentation. *Appl. Magn. Reson.* **37**, 795–818 (2010).
49. V. Stepanov, F. H. Cho, C. Abeywardana, S. Takahashi, High-frequency and high-field optically detected magnetic resonance of nitrogen-vacancy centers in diamond. *Appl. Phys. Lett.* **106**, 063111 (2015).
50. M. Schubert, S. Knight, S. Richter, P. Kühne, V. Stanishev, A. Ruder, M. Stokey, R. Korlacki, K. Irmscher, P. Neugebauer, V. Darakchieva, Terahertz electron paramagnetic resonance generalized spectroscopic ellipsometry: The magnetic response of the nitrogen defect in 4H-SiC. *Appl. Phys. Lett.* **120**, 102101 (2022).
51. N. Abhyankar, A. Agrawal, J. Campbell, T. Maly, P. Shrestha, V. Szalai, Recent advances in microresonators and supporting instrumentation for electron paramagnetic resonance spectroscopy. *Rev. Sci. Instrum.* **93**, 101101 (2022).
52. G. R. Eaton, S. S. Eaton, Rapid-scan electron paramagnetic resonance. *eMagRes* **5**, 1529–1542 (2016).
53. S. S. Eaton, R. W. Quine, M. Tseitlin, D. G. Mitchell, G. A. Rinard, G. R. Eaton, "Rapid-scan electron paramagnetic resonance," in *Multifrequency Electron Paramagnetic Resonance* (John Wiley & Sons Ltd., 2014), pp. 3–67.
54. T. S. Braun, J. Stehle, S. Kacprzak, P. Carl, P. Höfer, V. Subramaniam, M. Drescher, Intracellular protein–lipid interactions studied by rapid-scan electron paramagnetic resonance spectroscopy. *J. Phys. Chem. Lett.* **12**, 2471–2475 (2021).
55. J. Dröden, M. Drescher, Rapid scan electron paramagnetic resonance spectroscopy is a suitable tool to study intermolecular interactions of intrinsically disordered protein. *Biology* **12**, 79 (2023).
56. P. F. Goldsmith, *Quasioptical Systems* (Chapman & Hall, 1998).
57. P. Cruz, E. D. Shoemake, P. Adam, J. Leachman, Tensile strengths of polyamide based 3D printed polymers in liquid nitrogen. *IOP Conf. Ser. Mater. Sci. Eng.* **102**, 012020 (2015).
58. S. Maity, B. D. Price, C. B. Wilson, A. Mukherjee, M. Starck, D. Parker, M. Z. Wilson, J. E. Lovett, S. Han, M. S. Sherwin, Triggered functional dynamics of AsLOV2 by time-resolved electron paramagnetic resonance at high magnetic fields. *Angew. Chem. Int. Ed.* **62**, e202212832 (2023).
59. M. Afeworki, N.-R. Miller, N. Devasahayam, J. Cook, J.-B. Mitchell, S. Subramanian, M.-C. Krishna, Preparation and EPR studies of lithium phthalocyanine radical as an oxymetric probe. *Free Radic. Biol. Med.* **25**, 72–78 (1998).
60. C. B. Wilson, thesis, University of California, Santa Barbara, Santa Barbara, CA (2019).
61. G. Ilangovan, J. L. Zweier, P. Kuppusamy, Mechanism of oxygen-induced EPR line broadening in lithium phthalocyanine microcrystals. *J. Magn. Reson.* **170**, 42–48 (2004).
62. E. Bartolomé, B. Bozzo, P. Sevilla, O. Martínez-Pasarell, T. Puig, X. Granados, ABS 3D printed solutions for cryogenic applications. *Cryogenics* **82**, 30–37 (2017).
63. P. Turek, J.-J. André, A. Giraudeau, J. Simon, Preparation and study of a lithium phthalocyanine radical: Optical and magnetic properties. *Chem. Phys. Lett.* **134**, 471–476 (1987).
64. M. Tseytlin, General solution for rapid scan EPR deconvolution problem. *J. Magn. Reson.* **318**, 106801 (2020).
65. G. Latmiral, A. Sposito, Radar corner reflectors for linear or circular polarization. *J. Res. Nat. Bur. Sta.* **66**, 23 (1962).
66. W. A. Challener, Achromatic 90° polarization rotating prisms. *Appl. Opt.* **35**, 6845–6846 (1996).
67. G. M. Smith, J. C. G. Lesurf, R. H. Mitchell, P. C. Riedi, Quasi-optical cw mm-wave electron spin resonance spectrometer. *Rev. Sci. Instr.* **69**, 3924 (1998).
68. D. E. Budil, Z. Ding, G. R. Smith, K. A. Earle, Jones Matrix formalism for quasioptical EPR. *J. Magn. Reson.* **144**, 20–34 (2000).
69. D. T. Chuss, E. J. Wollack, S. H. Moseley, G. Novak, Interferometric polarization control. *Appl. Optics* **45**, 5107–5117 (2006).
70. A. Schillaci, P. de Bernardis, On the effect of tilted roof reflectors in Martin–Puplett spectrometers. *Infrared. Phys. Technol.* **55**, 40–44 (2012).
71. G. M. Smith, P. A. S. Cruickshank, D. R. Bolton, D. A. Robertson, High-field pulse EPR instrumentation. *J. Magn. Reson.* **21**, 216–233 (2008).
72. D. T. Teaney, M. P. Klein, A. M. Portis, Microwave superheterodyne induction spectrometer. *Rev. Sci. Instrum.* **32**, 721–729 (1961).
73. M. R. Fuchs, T. F. Prisner, K. Mobius, A high-field/high-frequency heterodyne induction-mode electron paramagnetic resonance spectrometer operating at 360 GHz. *Rev. Sci. Instrum.* **70**, 3681–3683 (1999).
74. E. J. Wollack, S. H. Moseley, G. A. Novak, D. T. Chuss, Interferometric polarization control. U.S. Patent 20080231529A1 (2009).
75. A. Sojka, M. Sedivy, A. Lagin, A. Gabris, T. Laznicka, V. T. Santana, O. Laguta, P. Neugebauer, Sample holders for sub-THz electron spin resonance spectroscopy. *IEEE Trans. Instrum. Meas.* **71**, 1–12 (2022).

Acknowledgments: We would like to thank N. Agladze for insight regarding quasi-optical design and assistance with Gaussian beam propagation simulations. **Funding:** This work was supported by the National Science Foundation, grants DMR 2117994 (M.S., S.H., and R.C.) and MCB 2025860 (M.S. and S.H.). **Author contributions:** Conceptualization: A.S. Methodology: A.S. and B.D.P. Investigation: A.S. and B.D.P. Visualization: A.S. and B.D.P. Supervision: M.S.S. Writing—original draft: A.S. and B.D.P. Writing—review and editing: A.S., B.D.P., and M.S.S. **Competing interests:** The authors declare that they have no competing interests. **Data and materials availability:** All data needed to evaluate the conclusions in the paper are present in the paper and/or the Supplementary Materials. Original data and processing scripts are available at doi.org/10.5281/zenodo.8169993.

Submitted 18 May 2023
Accepted 18 August 2023
Published 20 September 2023
10.1126/sciadv.adi7412